

A HYBRID REDUCED ORDER METHOD FOR MODELLING TURBULENT HEAT TRANSFER PROBLEMS

SOKRATIA GEORGAKA^{1,*}, GIOVANNI STABILE², KELBIJ STAR^{3,4}, GIANLUIGI ROZZA², AND MICHAEL J. BLUCK¹

ABSTRACT. A parametric, hybrid reduced order model approach based on the Proper Orthogonal Decomposition with both Galerkin projection and interpolation based on Radial Basis Functions method is presented. This method is tested against a case of turbulent non-isothermal mixing in T-junction pipe, a common flow arrangement found in nuclear reactor cooling systems. The reduced order model is derived from the 3D unsteady, incompressible Navier-Stokes equations weakly coupled with the energy equation. For high Reynolds numbers, the eddy viscosity and eddy diffusivity are incorporated into the reduced order model with a Proper Orthogonal Decomposition (nested and standard) with Interpolation (PODI), where the interpolation is performed using Radial Basis Functions. Two full-order turbulent modelling techniques, the Large Eddy Simulation (LES) and the Unsteady Reynolds Averaged Navier-Stokes Equations (URANS) are compared showing that the former requires fewer modes for the eddy viscosity field. The reduced order solver, obtained using a URANS full order model, is tested against the full order solver in a 3D T-junction pipe with parametric velocity inlet boundary conditions.

1. INTRODUCTION

The simulation of realistic large-scale many-query systems and the use of real-time control is an ambition in almost every industry. These large-scale systems are usually governed by partial differential equations (PDEs) which are complex and generally nonlinear. In the case of parametric PDEs, which are essential in design, control and optimisation, such large scale systems need to be solved for a large range of parameter values. As a consequence, their solution requires great computational effort, even with the use of state-of-the art computers and sophisticated computational libraries. A motivating example of this type of challenge can be found in the nuclear industry where a variety of phenomena, including turbulent flows, multiphase flows and heat transfer occur in complex geometries and therefore, obtaining high fidelity solutions across a wide range of scenarios becomes an unfeasible task without considerable simplification.

Reduced Order Models (ROMs) have been proposed as a way of overcoming the computational burden required to obtain high fidelity solutions in large-scale systems. The basic principle of many ROMs is that the full order solution can be approximated using only a linear combination of 'dominant' modes. The procedure entails two stages: some typically expensive 'offline' calculations and inexpensive online calculations. In non-parametric transient cases, the Reduced Order Model (ROM) coefficients are only time

dependent. In transient parametric cases, in the offline stage, the ROM is also trained on a set of different geometrical or physical parameter values, where as a result, a low-dimensional basis is computed. In the online stage, the ROM can be used for evaluating solutions on non-trained points in the parameter space or for time evolution if non-parametric PDEs are of interest. This process is achieved by projecting the full order equations (e.g. the Navier-Stokes equations) onto the calculated low-dimensional basis. An extensive review on projection-based ROMs can be found in [9].

In this work, the interest is focused on a hybrid POD - Galerkin - Proper Orthogonal Decomposition with Interpolation (PODI) based on Radial Basis Function method for parametric, time dependent PDEs governing turbulent fluid flow for non-isothermal mixing problems. POD-Galerkin has been applied to non-parametric PDEs with success across a wide range of applications. Beginning with the POD, this method was originally conceived as a method for compressing large datasets. An overview of POD can be found in [21]. In the field of fluid dynamics, Lumley [36] was the first to apply POD to the study of turbulent flows. Later, Sirovich [51] proposed an 'optimised' method of performing the POD, known as the snapshot POD, where large data sets which are usually arising from large scale systems are available. Other applications of POD can be found in [7, 10, 45].

¹IMPERIAL COLLEGE LONDON, DEPARTMENT OF MECHANICAL ENGINEERING, LONDON, SW7 2BX, UK.

²SISSA, INTERNATIONAL SCHOOL FOR ADVANCED STUDIES, MATHEMATICS AREA, MATHLAB TRIESTE, ITALY.

³INSTITUTE FOR ADVANCED NUCLEAR SYSTEMS, SCK-CEN, MOL, BELGIUM.

⁴DEPARTMENT OF FLOW, HEAT AND COMBUSTION MECHANICS, GHENT UNIVERSITY, GHENT, BELGIUM.

E-mail addresses: s.georgaka16@imperial.ac.uk, gstable@sisssa.it, kelbij.star@sckcen.be, rozza@sisssa.it, m.bluck@imperial.ac.uk.

Key words and phrases. proper orthogonal decomposition; Galerkin; finite volume approximation; heat transfer; radial basis functions; nested proper orthogonal decomposition; Navier-Stokes equations.

*Corresponding Author.

The idea of PODI method, which was introduced by Buihanh in [14], is based on the calculation of the POD coefficients using an interpolation technique. This method has been applied in aerodynamics in [23] and in [49] for parametrised geometries, as well as in cardiac mechanics in [43].

The use of POD methods with Galerkin projection fall into the category of projection-based ROMs and has been applied in various areas for incompressible [44, 11, 35] and compressible flows [8, 46]. In regard to parametric PDEs, which are the main interest of this study, POD-Galerkin has been applied in [6] where the authors proposed a monolithic reduced order modelling approach for parametrised fluid-structure interaction problems. Also in [5], a stable POD-Galerkin method for the parametrised, incompressible steady Navier-Stokes equation is presented. Stabile *et al* in [55] applied a POD-Galerkin ROM to the parametrised, incompressible unsteady Navier-Stokes equations. A POD-Galerkin model order reduction for parametric PDEs is also found in the study of haemodynamics in the work of Ballarin *et al* [3]. In [29] and [30], Hijazi *et al* developed a POD-Galerkin ROM method for parametric Navier-Stokes equations in the turbulent regime while in [53] the authors focused on turbulence closure using VMS techniques. Another approach which uses Petrov-Galerkin projection for efficient nonlinear model order reduction is presented in [17, 62, 18].

In this work, the 3D, parametric, transient Navier-Stokes equations, weakly coupled with the energy equation are considered. In particular, the method presented in this work is applied to the modelling of turbulent thermal mixing in a T-junction pipe, a configuration commonly found in nuclear power reactor cooling systems and which plays a crucial role in the safety of reactors. The mixing of two different temperature streams leads to high transient temperature fluctuations in the pipe wall regions which can potentially lead to thermal fatigue and subsequent failure of the piping material (cracks formation, breakage etc). Turbulent thermal mixing has been studied both experimentally and computationally in [25, 60, 38, 2, 57, 34]. In the computational case, various turbulent modelling techniques have been studied, including Large Eddy Simulation (LES) and Unsteady Reynolds Averaged Navier-Stokes (URANS). These methods, given the high Reynold's numbers and the nature of the problem, require fine 3D meshes which lead to very high CPU and memory costs. A ROM could therefore play a key role in such studies, giving the ability to obtain fast and reliable simulations. Model order reduction for nuclear applications has been previously applied in [50] for modelling the movement of the control rods in a nuclear reactor and in [13] for reactor critically problems. This work extends the previous work of [26] from laminar to turbulent heat transfer case. Other applications on POD-Galerkin ROM for coupled Navier-Stokes and energy equations include the work of Busto *et al* [15] as well as in [42]. To the best of the authors knowledge, a ROM for modelling the parametric 3D Navier-Stokes equations, weakly coupled

with the energy equation, including turbulence modelling is presented here for the first time. For the calculation of the reduced basis, two approaches are compared: a standard POD and a nested POD method. For the eddy viscosity term, an approach similar to the one developed in [29, 30] is followed. This approach is based on the use of PODI with Radial Basis Function (RBF) interpolation for the calculation of the temporal coefficients of the eddy viscosity term. The POD-RBF method has been previously applied in the model order reduction context in [22] as a non-intrusive model order reduction method as well as in [63] for multi-phase flow in porous media. In [40], a POD-RBF network for inverse heat conduction problems is presented.

This paper is organised as follows: in 2 the mathematical formulation is presented and in 3 the reduced order method is developed. In 4.1 a comparative study between LES and URANS turbulent modelling techniques and the effects on the ROM is presented. In 4.2, the ROM is tested on a case of turbulent thermal mixing in a T-junction pipe. In the final section, 5 conclusions and perspectives are drawn, highlighting the directives for future improvements and developments.

2. FULL ORDER MODEL - MATHEMATICAL BACKGROUND

In this section, the mathematical formulation of the FOM is presented. We consider the three dimensional, incompressible, transient, parametric Navier-Stokes equations weakly coupled with a three dimensional transient, parametric transport equation for heat. Since we are considering turbulent flows, some relevant background in turbulence modelling is presented.

2.1. Turbulence Modelling. Turbulence is described by chaotic and random motions where the transported quantities (pressure, velocity etc) exhibit spatial and temporal fluctuations. Unlike laminar flows which can be directly numerically solved by many discretisation techniques (e.g. finite volume), practical modelling of turbulent flows involves additional approximations. While there is no exact delineation, a flow is usually considered turbulent if the non-dimensional Reynolds number, $Re > 4000$, laminar if $Re < 2300$ and transitional when $2300 < Re < 4000$. The Reynolds number indicates the relative significance of the inertia forces in comparison to viscous forces. Turbulent motion greatly increases the effective diffusivity which leads to enhanced mixing, resulting in greater heat and momentum transfer.

In the modelling of turbulent flows, the instantaneous velocity component $\mathbf{u}(\mathbf{x}, t)$ is decomposed into a time-averaged component $\bar{\mathbf{u}}(\mathbf{x}, t)$ and a fluctuating component $\mathbf{u}'(\mathbf{x}, t)$, which can be expressed as:

$$(1) \quad \mathbf{u}(\mathbf{x}, t) = \bar{\mathbf{u}}(\mathbf{x}, t) + \mathbf{u}'(\mathbf{x}, t).$$

The fluctuating component in the above equation (1) is known as the turbulent fluctuation and is always three dimensional (in space), even for flows where the mean values

change only in two dimensions. Turbulent flows contain rotational flow structures, the turbulent eddies, which vary in size. Larger eddies, acquire energy from the mean flow by a process called vortex stretching. The smaller eddies derive energy from the larger eddies through an energy cascade process and viscous dissipation converts turbulent energy from the smallest eddies (0.1-0.01mm - Kolmogorov microscales) into thermal internal energy leading to energy losses.

Regarding turbulence modelling, there are various computational approaches. These approaches include the Reynolds-Averaged Navier-Stokes method (RANS or URANS for the unsteady case), Large Eddy Simulation (LES) and the most CPU expensive of all, Direct Numerical Simulation (DNS). RANS-URANS is the most widely used method in industry due to its relatively low computational cost in comparison with other methods for which the Navier-Stokes equations are solved in an averaged manner (ensemble or time). In LES the larger eddies are directly resolved whereas the smaller eddies (smaller than the mesh size) are modelled. LES has much greater computational cost than RANS and can be impractical for industrial applications. DNS numerically solves the Navier-Stokes equations and resolves the whole spectrum of eddies but this comes at vast computational cost.

In this work, only the first two methods will be considered, with a preference for URANS due to its applicability in industry and reduced computational effort. LES will only be considered for the purposes of a comparative study to show the dependence of the ROM, if any, to the different turbulence modelling techniques. Amongst the various methods available (Spalart-Almaras, $k - \epsilon$, $k - \omega$, Reynolds Stresses etc) in RANS/URANS, the $k - \omega$ is chosen due to its accuracy in the near wall region. There are two variations of the $k - \omega$ model, the standard $k - \omega$ and the Shear Stress Transport (SST) $k - \omega$. The former is described by a two-transport-equation model for k and ω and the specific dissipation rate (ϵ/k) is based on Wilcox [61]. The latter, is a combination of the standard $k - \omega$ model in proximity of the walls and the standard $k - \epsilon$ model in the bulk of the flow. To ensure smooth transition between the two different models, a blending function is used.

To derive the full-order equations which also include turbulence modelling, we start with the standard incompressible, transient parametric Navier-Stokes equations which are weakly coupled with the transient parametric heat transport equation. Considering an Eulerian framework and domain $\mathcal{Q} = \Omega \times [0, T_s] \subset \mathbb{R}^d \times \mathbb{R}^+$ with $d = 1, 2, 3$, the

equations are formulated as follow:

$$(2) \quad \begin{cases} \frac{\partial \mathbf{u}(\mathbf{x}, \boldsymbol{\mu}, t)}{\partial t} + \nabla \cdot (\mathbf{u}(\mathbf{x}, \boldsymbol{\mu}, t) \otimes \mathbf{u}(\mathbf{x}, \boldsymbol{\mu}, t)) - \\ - \nabla \cdot \nu \nabla \mathbf{u}(\mathbf{x}, \boldsymbol{\mu}, t) = -\nabla p(\mathbf{x}, \boldsymbol{\mu}, t) & \text{in } \mathcal{Q}, \\ \nabla \cdot \mathbf{u}(\mathbf{x}, \boldsymbol{\mu}, t) = \mathbf{0} & \text{in } \mathcal{Q}, \\ \frac{\partial \theta(\mathbf{x}, \boldsymbol{\mu}, t)}{\partial t} + \nabla \cdot (\mathbf{u}(\mathbf{x}, \boldsymbol{\mu}, t) \theta(\mathbf{x}, \boldsymbol{\mu}, t)) - \\ - \alpha_{dif} \Delta \theta(\mathbf{x}, \boldsymbol{\mu}, t) = 0 & \text{in } \mathcal{Q}, \\ \mathbf{u}(\mathbf{x}, \boldsymbol{\mu}) = \mathbf{f}(\mathbf{x}, \boldsymbol{\mu}) & \text{on } B_{In}, \\ \theta(\mathbf{x}, \boldsymbol{\mu}) = g(\mathbf{x}) & \text{on } B_{In}, \\ \nabla \theta(\mathbf{x}, \boldsymbol{\mu}) \cdot \mathbf{n} = 0 & \text{on } B_w, \\ \mathbf{u}(\mathbf{x}, \boldsymbol{\mu}) = \mathbf{0} & \text{on } B_w, \\ \nu (\nabla \mathbf{u} - p \mathbf{I}) \mathbf{n} = \mathbf{0} & \text{on } B_o, \\ \mathbf{u}(0, \mathbf{x}) = \mathbf{h}(\mathbf{x}) & \text{in } T_0, \\ \theta(0, \mathbf{x}) = e(\mathbf{x}) & \text{in } T_0, \end{cases}$$

where \mathbf{u} is the fluid velocity, p the normalised pressure, θ is the fluid temperature, α_{dif} is the thermal diffusivity and ν is the kinematic viscosity. The vector of parameters is represented by the greek letter $\boldsymbol{\mu}$. $B_{In} = \Gamma_{In} \times [0, T_s]$, $B_w = \Gamma_w \times [0, T_s]$ and $B_o = \Gamma_o \times [0, T_s]$, T_s represents the time-period of the simulation, $\Gamma = \Gamma_{In} \cup \Gamma_w \cup \Gamma_o$ is the boundary of \mathcal{Q} and consists of three different parts Γ_{In} , Γ_o and Γ_w that indicate, respectively, inlet(s), outlet and physical wall boundaries (2). The functions $\mathbf{f}(\mathbf{x}, \boldsymbol{\mu})$ and $g(\mathbf{x})$ represent the boundary conditions for the non-homogeneous boundaries. $\mathbf{h}(\mathbf{x})$ and $e(\mathbf{x})$ denote the initial conditions for velocity and temperature at $t = 0$. Time independence of the boundary conditions \mathbf{f} and g is also assumed. Since we are dealing with the incompressible equations, the density ρ has been omitted and is assumed to have the value of 1. In this work, the parametric dependency is on the velocity inlet boundary conditions.

Similar to equation (1) the instantaneous velocity, pressure and temperature can be written as:

$$\begin{aligned} (3) \quad & \mathbf{u}(\mathbf{x}, t) = \bar{\mathbf{u}}(\mathbf{x}, t) + \mathbf{u}'(\mathbf{x}, t) \\ (4) \quad & p(\mathbf{x}, t) = \bar{p}(\mathbf{x}, t) + p'(\mathbf{x}, t), \\ (5) \quad & \theta(\mathbf{x}, t) = \bar{\theta}(\mathbf{x}, t) + \theta'(\mathbf{x}, t). \end{aligned}$$

When using RANS modelling, the mean components of the fluctuating terms are zero. Taking this into account and substituting equations (3) into equations (2), the Reynolds-averaged Navier-Stokes and energy equations are:

$$(6) \quad \begin{cases} \nabla \cdot \bar{\mathbf{u}} = 0, \\ \frac{\partial \bar{\mathbf{u}}}{\partial t} + \nabla \cdot (\bar{\mathbf{u}} \otimes \bar{\mathbf{u}}) - \nu \Delta \bar{\mathbf{u}} = -\nabla \bar{p} - \nabla \cdot \boldsymbol{\tau}^R, \\ \frac{\partial \bar{\theta}}{\partial t} + \nabla \cdot (\bar{\mathbf{u}} \bar{\theta}) - (\alpha_{dif} \Delta \bar{\theta}) - \nabla \cdot \mathbf{H}^R = 0, \end{cases}$$

where the extra terms $\boldsymbol{\tau}^R = -(\overline{\mathbf{u}'\mathbf{u}'})$ and $\mathbf{H}^R = (\overline{\mathbf{u}\theta'}) - \bar{\mathbf{u}}\bar{\theta}$ are the Reynolds stress tensor and the heat flux term respectively. Therefore, these two new terms must be modelled in order to close the system of the equations. One possible solution, which we will follow here is the eddy viscosity models with the Boussinesq hypothesis. The Reynolds stress is modelled using an eddy viscosity ν_t

$$(7) \quad \boldsymbol{\tau}^R = -\overline{(\mathbf{u}'\mathbf{u}')} = 2\nu_t \overline{\mathbf{D}}^R - 2/3k\mathbf{I} = \nu_t[\nabla\bar{\mathbf{u}} + (\nabla\bar{\mathbf{u}})^T] - 2/3k\mathbf{I},$$

while the heat flux using a gradient diffusion hypothesis as follows:

$$(8) \quad \mathbf{H} = -\alpha_{dif_t} \nabla\bar{\theta},$$

where α_{dif_t} is the turbulent thermal diffusivity defined as ν_t/Pr_t and Pr_t the turbulent Prandtl, $\overline{\mathbf{D}}^R$ the Reynolds-averaged strain rate tensor and \mathbf{I} the identity matrix.

Combining all of the above and denoting from now on $\bar{\mathbf{u}}$, \bar{p} and $\bar{\theta}$ as \mathbf{u} , p and θ respectively, equations (2) including also the turbulence modelling are as follows:

$$(9) \quad \begin{cases} \frac{\partial \mathbf{u}}{\partial t} + \nabla \cdot (\mathbf{u} \otimes \mathbf{u}) = \nabla \cdot [(\nu + \nu_t) \cdot \frac{1}{2}(\nabla \mathbf{u} + (\nabla \mathbf{u})^T) - p\mathbf{I}], \\ \nabla \cdot \mathbf{u} = 0, \\ \frac{\partial \theta}{\partial t} + \nabla \cdot (\mathbf{u}\theta) - (\alpha_{dif} + \alpha_{dif_t})\Delta\theta = 0, \\ \nu_t = j(k, \omega), \\ \mathbf{u} = \mathbf{f} & \text{on } B_{In}, \\ \theta = g & \text{on } B_{In}, \\ \mathbf{u} = \mathbf{0} & \text{on } B_w, \\ \nabla\theta \cdot \mathbf{n} = 0 & \text{on } B_w, \\ \nu(\nabla\mathbf{u} - p\mathbf{I})\mathbf{n} = \mathbf{0} & \text{on } B_o, \\ \mathbf{u}(0) = \mathbf{h} & \text{in } T_0, \\ \theta(0) = e & \text{in } T_0, \end{cases}$$

within the space-time domain \mathcal{Q} . The turbulent kinetic energy is k , $k = \frac{1}{2}\mathbf{u} \cdot \mathbf{u}$ and $\omega = \frac{\epsilon}{k\beta^*}$ is the specific dissipation rate with β^* being a constant of proportionality and $\epsilon \propto \frac{\partial k}{\partial t}$ is the dissipation rate. For the k and ω transport equations the reader should refer to [59]. For brevity, the parametric, spatial and temporal dependency on the momentum, continuity and energy equations has been omitted.

2.2. Finite Volume Approximation. The full order partial differential equations (9) are transformed into a discrete system of algebraic equations using the finite volume method. The solution domain is discretised with the generation of a computational mesh in a number of arbitrary cells or control volumes over which the equations are solved (spatial discretisation) and the variables of interest are calculated at the centroid of the control volumes (1). The time is also discretised in a number of timesteps (temporal discretisation). The integral form of the equations are discretised over each cell so that, at the discrete level, the mass and momentum are conserved.

To give a brief description of the discretisation process, a general transport equation for a transported quantity ϕ , in a control volume Ω_i , where the density ρ is taken equal

to 1 and no sources are considered, can be expressed as:

$$(10) \quad \int_{\Omega_i} \frac{\partial \phi}{\partial t} d\Omega + \int_{\Omega_i} \nabla \cdot (\mathbf{u}\phi) d\Omega - \int_{\Omega_i} \nabla \cdot (\Gamma_\phi \nabla \phi) d\Omega = 0,$$

where Γ_ϕ is the diffusion coefficient of the transported quantity. The above transport equation (10) consists of 3 terms with the first one being the temporal term, the second one the convective term and the last one the diffusive term. As this equation is second order, a second or higher order discretisation scheme is needed. The volume integrals in the convective and diffusive terms are converted into surface integrals using Gauss theorem, which for a vector \mathbf{w} is:

$$(11) \quad \int_{\Omega_i} \nabla \cdot \mathbf{w} d\Omega = \oint_{\partial\Omega_i} \mathbf{n} dS \cdot \mathbf{w},$$

where \mathbf{n} denotes the normal vector pointing outward of the bounding surface $\partial\Omega_i$. The volume and surface integrals are then approximated by a discrete sum over the faces of the control volume Ω_i . The values on the faces of the control volume are calculated by interpolating the values from the adjacent control volumes. The most widely used interpolation schemes are the central differencing and upwind differencing schemes. Regarding the temporal term, there is also a variety of differencing schemes including the backward differencing scheme, Crank-Nicolson, Euler etc. For a detailed review on the finite volume discretisation the reader could refer to [37].

3. REDUCED ORDER MODEL FORMULATION

A POD-Galerkin method is used for the development of the ROM. We adopt a procedure similar to that used for the laminar case in [26], combined with the procedure first introduced in [29] for the modelling of the eddy viscosity term when high Reynolds numbers are considered. This method is extended to the modelling of the eddy diffusivity when the temperature transport equation is considered.

One can decompose the velocity, pressure and temperature fields as a linear combination of basis functions multiplied by temporal coefficients as follows:

$$(12) \quad \mathbf{u}(\mathbf{x}, \boldsymbol{\mu}, t) \approx \mathbf{u}_s = \sum_{i=1}^{N_u^s} \alpha_i(\boldsymbol{\mu}, t) \phi_i(\mathbf{x}),$$

$$(13) \quad p(\mathbf{x}, \boldsymbol{\mu}, t) \approx p_s = \sum_{i=1}^{N_p^s} b_i(\boldsymbol{\mu}, t) \psi_i(\mathbf{x}),$$

$$(14) \quad \theta(\mathbf{x}, \boldsymbol{\mu}, t) \approx \theta_s = \sum_{i=1}^{N_\theta^s} c_i(\boldsymbol{\mu}, t) \chi_i(\mathbf{x}),$$

where $\phi(\mathbf{x})$, $\psi(\mathbf{x})$ and $\chi(\mathbf{x})$ are spatial basis functions and $\alpha(\boldsymbol{\mu}, t)$, $b_i(\boldsymbol{\mu}, t)$ and $c_i(\boldsymbol{\mu}, t)$ are the temporal coefficients for the velocity, pressure and temperature fields respectively. N_u^s , N_p^s and N_θ^s is the cardinality of the POD spaces for velocity, pressure and temperature respectively. Considering the FOM, which exhibits parametric and temporal dependency, is solved for N_p training points of a parameter of interest $\boldsymbol{\mu}^p \in \mathcal{P} = \{\boldsymbol{\mu}^1, \dots, \boldsymbol{\mu}^N\}$ and for N_t time

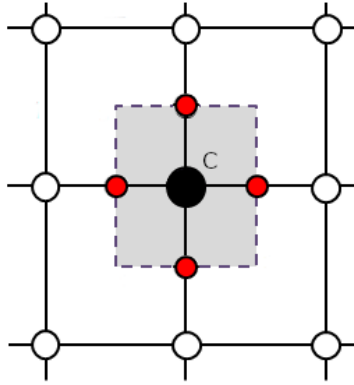


FIGURE 1. A 2D control volume with C being the centroid of the volume.

instances, $t^k \in \{t^1, \dots, t^k\} \subset [0, T_s]$. Therefore, the total number of velocity snapshots is $N_u^s = N_p \times N_t$.

For turbulent modelling, a new term is introduced which approximates the eddy viscosity term:

$$(15) \quad \nu_t(\mathbf{x}, \boldsymbol{\mu}, t) \approx \nu_{t_s} = \sum_{i=1}^{N_{\nu_t}^s} l_i(\boldsymbol{\mu}, t) \xi_i(\mathbf{x}),$$

where $\xi(\mathbf{x})$ and $l(\boldsymbol{\mu}, t)$ represent the basis functions and the temporal coefficients for the eddy viscosity field.

The basis functions are calculated using the POD method for parametric problems, where an equispaced grid sampling over a range of parameters and time is performed. This results to a global snapshot matrix which contains both parameter and time information. Therefore, for the velocity, the snapshot matrix, \mathbf{U}_s , is formed as

$$\mathbf{U}_s = \begin{bmatrix} u_1^1(\mu^1) & \dots & u_1^{N_t}(\mu^1) & \dots & u_1^{N_t}(\mu^{N_p}) \\ \vdots & \dots & \vdots & \dots & \vdots \\ u_{N_u^h}^1(\mu^1) & \dots & u_{N_u^h}^{N_t}(\mu^1) & \dots & u_{N_u^h}^{N_t}(\mu^{N_p}) \end{bmatrix},$$

where N_u^h are the number of degrees of freedom which is equal to the number of grid points times the number of the components. For any vector or scalar function \mathbf{w} , the POD method seeks to find an orthonormal basis $\boldsymbol{\phi}(\mathbf{x})$ of rank N_w^r which minimises the quantity:

$$(16) \quad \arg \min \sum_{i=1}^{N_w^s} \left\| \mathbf{w}_i - \sum_{j=1}^{N_w^r} \langle \mathbf{w}_i(\mathbf{x}, \boldsymbol{\mu}, t), \boldsymbol{\phi}_j(\mathbf{x}) \rangle_{L_2(\Omega)} \boldsymbol{\phi}_j(\mathbf{x}) \right\|_{L_2}^2,$$

with,

$$(17) \quad \langle \boldsymbol{\phi}_i, \boldsymbol{\phi}_j \rangle_{L_2(\Omega)} = \delta_{ij}, \forall i, j = 1, \dots, N_w^s.$$

The vector function \mathbf{w} can be the velocity vector $\mathbf{u}(\mathbf{x}, \boldsymbol{\mu}, t)$ or the scalar functions for temperature $\theta(\mathbf{x}, \boldsymbol{\mu}, t)$ and pressure $p(\mathbf{x}, \boldsymbol{\mu}, t)$. The above problem (16) is equivalent to solving the eigenvalue problem:

$$(18) \quad \mathbf{C}\mathbf{W} = \mathbf{W}\boldsymbol{\lambda},$$

$$(19) \quad C_{ij} = \langle \mathbf{u}_i, \mathbf{u}_j \rangle_{L_2(\Omega)}, \forall i, j = 1, \dots, N_u^s,$$

where \mathbf{C} is the correlation matrix, \mathbf{W} a matrix with the eigenvectors and $\boldsymbol{\lambda}$ a diagonal matrix with the eigenvalues.

The original POD basis, $\mathcal{V}_{POD} = \text{span}[\boldsymbol{\phi}_1, \boldsymbol{\phi}_2, \dots, \boldsymbol{\phi}_{N_u^s}]$ can be truncated according to the following energy criterion:

$$(20) \quad E_{N_u^r} = \frac{\sum_{i=1}^{N_u^r} \lambda_i}{\sum_{j=1}^{N_u^s} \lambda_j},$$

where λ_i are the eigenvalues and $N_u^r \ll N_u^s$ denotes the cardinality of the reduced POD space \mathcal{V}_{POD_r} .

The orthogonal POD basis functions, $\boldsymbol{\phi}(\mathbf{x})$, are calculated and normalised as:

$$(21) \quad \boldsymbol{\phi}_j = \frac{1}{\sqrt{\lambda_j N_u^r}} \sum_{i=1}^{N_u^r} \mathbf{u}_i \mathbf{W}_{ij},$$

$$(22) \quad \langle \boldsymbol{\phi}_i, \boldsymbol{\phi}_j \rangle_{L_2(\Omega)} = \delta_{ij} \quad \forall i, j = 1, \dots, N_u^r.$$

Other methods for the generation of the snapshot matrix include, for example, Greedy POD [28, 58], the goal-oriented POD-greedy sampling [31], the Proper Generalised Decomposition (PGD) [19], the nested POD [12] as well as other approaches, [47, 19, 33, 41, 20, 24]. In this work, the nested POD will be tested against the standard POD method.

3.1. Nested POD. The standard POD method becomes too expensive for training spaces with many training points as this leads to large dense matrix eigenproblems. Considering for example the velocity snapshots, the computational effort need for the solution of the quadratic eigenvalue problem, (18), scales with $\mathcal{O}([N_u^s]^3)$. The nested POD method approximates the global POD space by solving one small eigenvalue problem for each local parameter space. The local POD bases are then weighted by the eigenvalues and a global snapshot matrix is created by appending the local weighted POD basis. A standard POD is then performed on the global snapshot matrix and the basis is calculated according to the method described in (3). The advantage of the nested POD is the numerical efficiency over the standard POD method since the computational effort for the former scales as $\mathcal{O}([N_t^3 \cdot N_p + [N_u^{nested}]^3])$, where N_u^{nested} is the dimension of the global snapshot matrix resulting from the nested POD.

The nested POD acts on the following N_p local matrices:

$$\mathbf{U}_{nested}^i = \begin{bmatrix} u_1^1(\mu^i) & u_1^2(\mu^i) & \dots & u_1^{N_t}(\mu^i) \\ \vdots & \vdots & \dots & \vdots \\ u_{N_u}^1(\mu^i) & u_{N_u}^2(\mu^i) & \dots & u_{N_u}^{N_t}(\mu^i) \end{bmatrix},$$

where i runs from 1 to N_p . A POD is then performed on each local matrix \mathbf{U}_{nested}^i and we obtain corresponding local bases.

The global POD matrix is then formed by selecting the first N_t^{rn} modes from each local POD basis according to the energy criterion (20), weighted by their eigenvalues. The concatenation of the weighted modes results in the following global POD matrix:

$$\mathbf{U}_{s_n} = \begin{bmatrix} \lambda_1^1 \phi_1^1(\mu^1) & \dots & \lambda_1^{N_t^{rn}} \phi_1^{N_t^{rn}}(\mu^1) & \dots & \lambda_1^1 \phi_1^{N_t^{rn}}(\mu^{N_p}) \\ \vdots & \dots & \vdots & \dots & \vdots \\ \lambda_1^1 \phi_{N_u}^1(\mu^1) & \dots & \lambda_1^{N_t^{rn}} \phi_{N_u}^{N_t^{rn}}(\mu^1) & \dots & \lambda_1^1 \phi_{N_u}^{N_t^{rn}}(\mu^{N_p}) \end{bmatrix}.$$

Once the snapshot matrix \mathbf{U}_{s_n} is formed, the procedure is the same as that described in section (3).

3.2. Galerkin Projection. For the calculation of the temporal coefficients, a Galerkin approach is followed for the velocity, pressure and temperature fields, where the original equations are projected onto the reduced basis. The momentum equation is projected onto the spatial POD basis $\phi(\mathbf{x})$ while the continuity equation is projected onto the pressure spatial basis $\psi(\mathbf{x})$, using the supremizer method [48, 4]. The energy equation is projected onto the temperature spatial basis $\chi(\mathbf{x})$. The projection results in a set of ordinary differential equations showing the evolution of the temporal coefficients for velocity, pressure and temperature:

$$\mathbf{M}\dot{\boldsymbol{\alpha}} - \boldsymbol{\alpha}^T \mathbf{Q}\boldsymbol{\alpha} + (\nu + \nu_t) \mathbf{l}^T (\mathbf{Q}_{T1} + \mathbf{Q}_{T2}) \boldsymbol{\alpha} - \mathbf{P}\mathbf{b} = 0, \quad (24)$$

$$\mathbf{R}\boldsymbol{\alpha} = 0, \quad (25)$$

$$\mathbf{K}\dot{\mathbf{c}} - \boldsymbol{\alpha}^T \mathbf{G}\mathbf{c} - \alpha_{diff} \mathbf{N}\mathbf{c} = 0, \quad (26)$$

where the dotted terms $\dot{\boldsymbol{\alpha}}$ and $\dot{\mathbf{c}}$ represent time derivatives and the reduced matrices are:

$$(\mathbf{M})_{ij} = \langle \phi_i, \phi_j \rangle_{L_2(\Omega)}, \quad (27)$$

$$(\mathbf{Q})_{ijk} = \langle \nabla \cdot (\phi_i \otimes \phi_j), \phi_k \rangle_{L_2(\Omega)}, \quad (28)$$

$$(\mathbf{Q})_{T1ijk} = \langle \xi_i \Delta \phi_j, \phi_k \rangle_{L_2(\Omega)}, \quad (29)$$

$$(\mathbf{Q})_{T2ijk} = \langle \nabla \cdot \xi_i (\nabla \phi_j^T), \phi_k \rangle_{L_2(\Omega)}, \quad (30)$$

$$(\mathbf{P})_{ij} = \langle \nabla \psi_i, \phi_j \rangle_{L_2(\Omega)}, \quad (31)$$

$$(\mathbf{R})_{ij} = \langle \nabla \cdot \phi_i, \psi_j \rangle_{L_2(\Omega)}, \quad (32)$$

$$(\mathbf{K})_{ij} = \langle \chi_i, \chi_j \rangle_{L_2(\Omega)}, \quad (33)$$

$$(\mathbf{G})_{ijk} = \langle \nabla \cdot (\phi_i \chi_j), \chi_k \rangle_{L_2(\Omega)}, \quad (34)$$

$$(\mathbf{N})_{ij} = \langle \Delta \chi_i, \chi_j \rangle_{L_2(\Omega)}.$$

3.3. Radial Basis Functions. Considering the eddy viscosity field, the vector of temporal coefficients $\mathbf{l}(t)$ is computed using the non-intrusive method of Radial Basis Function (RBF) interpolation according to the procedure described in [29]. In this way, since there is no projection

of the eddy viscosity modes onto the turbulence modelling equations, the ROM is independent of the turbulent method which are used in the FOM.

The temporal coefficients, $l(\boldsymbol{\mu}, t)$, for a new value of the parameter, are calculated during the online stage as a linear combination of $N_{\nu_t}^s$ ($j = 1, 2, \dots, N_{\nu_t}^s$) chosen radial basis functions kernels Θ :

$$l_i(\boldsymbol{\mu}, t) = \sum_{j=1}^{N_{\nu_t}^s} w_{i,j} \Theta_{i,j}(\|\boldsymbol{\mu} - \boldsymbol{\mu}_j\|_{L_2}), \quad \text{for } i = 1, 2, \dots, N_{\nu_t}^s, \quad (35)$$

where, \mathbf{w} represents the vector of the linear weights, $\boldsymbol{\mu}$ are the sampling points (centers) corresponding to eddy viscosity snapshots ν_t and $\boldsymbol{\mu}$ is the value of the new input parameter which does not coincide with any of the training points. For the RBFs, Θ , various kernels can be used. In this work, Gaussian kernels are considered, defined as follow:

$$\Theta(\|\boldsymbol{\mu} - \boldsymbol{\mu}_j\|_{L_2}) = \exp(-\gamma \|\boldsymbol{\mu} - \boldsymbol{\mu}_j\|_{L_2}^2), \quad (36)$$

where γ is a parameter which determines the spread of the kernel. The RBF monotonically decreases as we move away from the centre. Gaussian RBFs response is local, meaning that their response is the best in the area near to the centre, in contrast to multiquadratic RBFs which are global. The unknowns are computed in the offline stage.

The vector of the weights is calculated by solving the following linear system:

$$\sum_{j=1}^{N_{\nu_t}^s} w_{i,j} \Theta_{i,j}(\|\boldsymbol{\mu}_k - \boldsymbol{\mu}_j\|_{L_2}) = l(\boldsymbol{\mu}, t)_{i,k}, \quad \text{for } k = 1, 2, \dots, N_{\nu_t}^s. \quad (37)$$

The above equation can be written in matrix form and solved for the unknown weights as:

$$\Theta \mathbf{w} = \mathbf{l} \Leftrightarrow \mathbf{w} = \Theta^{-1} \mathbf{l}, \quad (38)$$

provided that the matrix Θ is non-singular, therefore invertible and the temporal coefficients, $l(\boldsymbol{\mu}, t)_{i,j}$, are calculated by projecting the eddy viscosity snapshots onto the spatial eddy viscosity modes as:

$$l_{i,j}(\boldsymbol{\mu}, t) = \langle \xi_i, \nu_{t_j} \rangle_{L_2(\Omega)}, \quad \text{for } j = 1, 2, \dots, N_{\nu_t}^s. \quad (39)$$

Once the unknown weights are calculated, the system of equations (23), is ready to be solved.

3.4. Treatment of Boundary Conditions. The interest in the present work is the construction of a ROM with parametric boundary conditions. This means that, given a proper sampling of a given parameter, the ROM would be capable of simulating cases for new, untrained values of the chosen parameter provided these values belong to the training manifold. To achieve this property, a similar procedure to that introduced in [27] is followed.

This method first employs a control function to make the snapshots homogeneous and independent of the boundary conditions by subtracting the inhomogeneous boundary

value and then, at the reduced order level, the new boundary value is enforced and the contribution of the control function values is added back. Taking as example the velocity snapshots, these are homogenised as :

$$(40) \quad \mathbf{u}'(\mathbf{x}, \boldsymbol{\mu}, t) = \mathbf{u}(\mathbf{x}, \boldsymbol{\mu}, t) - \sum_{j=1}^{N_{BC}} u_{D_j}(\boldsymbol{\mu}, t) \boldsymbol{\zeta}_{c_j},$$

where N_{BC} is the number of parametrised boundary conditions and u_D are scaling coefficients that make the snapshots homogeneous. The control functions, $\boldsymbol{\zeta}$, are calculated by assigning:

$$(41) \quad \boldsymbol{\zeta}_c = \begin{cases} 1, & \text{at the Dirichlet boundary} \\ 0, & \text{on the other boundaries,} \end{cases}$$

and then are computed as $\boldsymbol{\zeta}_c = \frac{1}{N_u^s} \sum_{l=1}^{N_u^s} \mathbf{u}_l$ by solving a full order model. The POD is then applied to the homogeneous snapshots and the velocity field is approximated as:

$$(42) \quad \mathbf{u}(\mathbf{x}, \boldsymbol{\mu}, t) = \sum_{j=1}^{N_{BC}} u_{D_j}(\boldsymbol{\mu}, t) \boldsymbol{\zeta}_{c_j} + \sum_{i=1}^{N_u^s} \alpha_i(t, \boldsymbol{\mu}) \boldsymbol{\phi}_i(\mathbf{x}).$$

A similar procedure is followed for the temperature parametrised boundary conditions. For a detailed discussion the reader should refer to [54, 26].

4. APPLICATIONS

The mathematical framework described in the previous sections is tested on a 3D T-junction pipe, where different temperature water streams are mixing in the tee area at high Reynolds number. The boundary of the domain Ω , denoted with Γ consists of four parts, $\Gamma = \Gamma_m \cup \Gamma_b \cup \Gamma_w \cup \Gamma_o$ as shown in figure 2. The geometrical properties of the pipe are shown in table 1 and the total length of the pipe is $L = 3.0\text{m}$. First, a grid convergence study is performed for LES and URANS (figures 4 and 5) and a comparison between LES and $k-\omega$ SST URANS has been performed for various mesh sizes. The aim of this comparison is to investigate how the mesh size affects the number of POD modes corresponding to approximately 99.9% of the energy of the system, in each case.

4.1. Comparison between URANS and LES. A comparison of the decay of the POD modes between URANS and LES subgrid-scale (SGS) is presented in this section. The Reynolds number for the main pipe is $Re_m = 140000$ and for the branch pipe $Re_b = 160000$ and the velocities are $\mathbf{u}_m = 0.1\text{m/s}$ and $\mathbf{u}_b = 0.2\text{m/s}$, respectively. The mesh size is varied between 51324 and 568496 hexahedral cells. According to tables 2 and 3, given the same grid resolution, the number of modes for the eddy viscosity field (referred as "nut" field in figures) that contain a cumulative energy of approximately 99.9% are significantly less in the case of LES. This could be a consequence of LES being able to resolve most of the scales while, in RANS, only the largest eddies are resolved and the smallest eddies are modelled.

According to figure 6, the dominant POD mode (mode 1) contains much more energy in the case of LES than URANS. In fact, for ROMs constructed using LES training data, only a single eddy viscosity mode is needed as the mesh resolution improves. Velocity and pressure modes in case of LES appear to decay slower than in the case of RANS while the supremizer and temperature modes have almost the same rate of decay.

4.2. Nested and Standard POD methods. In this subsection, a comparison between nested POD and standard POD methods is presented. Since our interest is on the comparison between two different computational approaches: the full order (FOM) simulation performed in OpenFOAM [1] and the reduced order (ROM) simulation performed in ITHACA-FV C++ library [52], the chosen computational mesh consists of 291816 cells (hexahedra) for time-saving reasons. For a more accurate FOM and hence a more accurate ROM, one could use a finer mesh. A parametric turbulent case is considered, where velocity inlet boundary condition on both inlets is parametrised. This example has been chosen as the parametric response is non-linear and a proper training is needed. The training space is constructed using 10 sets of sampling points for the two velocity inlets, as shown on table (5). The reduced order model is evaluated in a new set of values $U_m = 0.132\text{ m/s}$ (main pipe) and $U_b = 0.264\text{ m/s}$ (branch pipe) which correspond to Reynolds numbers $Re_m = 184800$ and $Re_b = 211200$ for the main and branch pipes, respectively (see table (1)).

Regarding the offline phase, the FOM is modelled using the $k-\omega$ SST turbulence modelling with the transient pisoFoam solver [32]. The simulation time is set to 3s with timestep $dt = 0.0025\text{s}$. The spatial and temporal discretisation schemes are summarised on table (4). The FOM is run 10 times (one for each sampling pair) with snapshots being collected every 0.1s. This makes a total of $30 \cdot 10 = 300$ snapshots (30 snapshots per sampling pair) for each field. Therefore, $N_u^s = N_p^s = N_{sup}^s = N_\theta^s = N_{\nu_t}^s = 300$. The reduced basis, is computed with the POD method. Two different POD strategies are used: a standard POD and a nested POD. In the standard POD, the POD is applied directly on the global snapshots matrix which contains both parameter and time information in an equispaced grid, according to (3) and the reduced bases space is then chosen according to the decay of the eigenvalues shown in figure (7). The retained modes are 14 for velocity, 7 for pressure and supremizer, 8 for the eddy viscosity and 9 modes for temperature.

In the nested POD method, 10 local snapshot matrices are constructed (3.1), one for each sampling pair, and the POD is applied on each of them individually. The resulted bases functions are then truncated using the energy criterion (20) in order to retain approximately 99.9% of the total energy and the remained bases are weighted by their eigenvalues. According to this criterion, out of the 30 bases function, only 10 are retained and weighted for each sampling pair, giving a reduced dimension for the final global

	Main Pipe	Branch Pipe
u (m/s)	0.132	0.264
θ (K)	333.16	353.15
D (m)	0.14	0.08
Re	184800	211200

TABLE 1. Summary of the physical parameters for the reduced order model.

Mesh Size	u	θ	p	s	ν_t
51324	9	10	5	7	2
95952	10	10	5	7	2
291816	13	12	6	8	1
568496	15	14	7	8	1

TABLE 2. Number of cumulative POD Modes for velocity, temperature, pressure, supremizer and eddy viscosity fields, respectively, retaining approximately 99.9% of the total energy - LES case.

Mesh Size	u	θ	p	s	ν_t
51324	7	10	3	6	5
95952	8	10	3	7	5
291816	11	12	4	8	7
568496	12	14	4	8	7

TABLE 3. Number of cumulative POD Modes for velocity, temperature, pressure, supremizer and eddy viscosity fields, respectively, retaining approximately 99.9% of the total energy - URANS case.

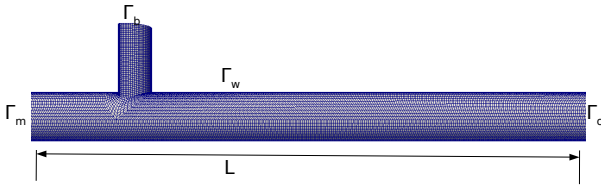


FIGURE 2. Computational mesh of the T-junction pipe.

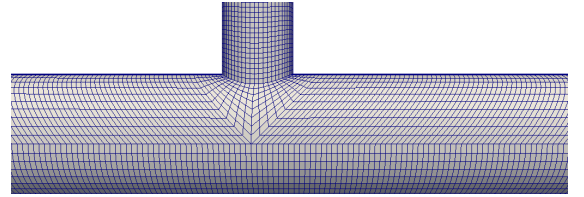


FIGURE 3. Mesh in T-junction region.

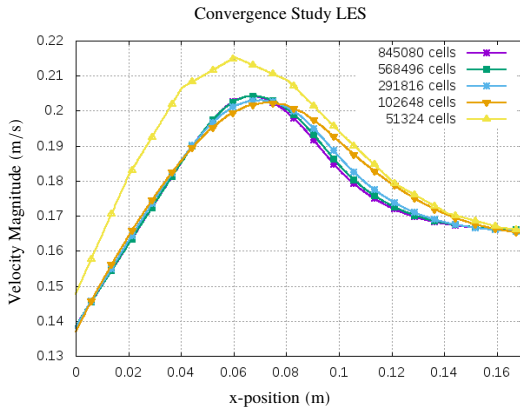


FIGURE 4. Grid convergence study for LES.

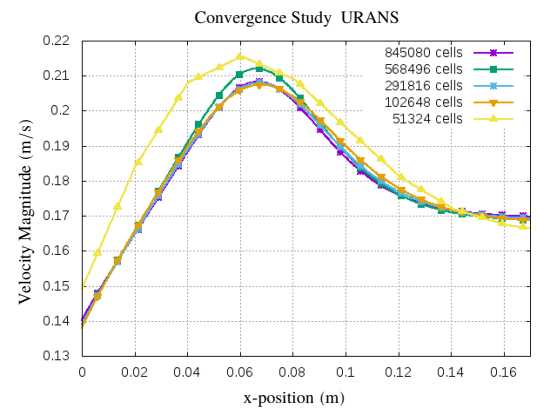


FIGURE 5. Grid convergence study for URANS.

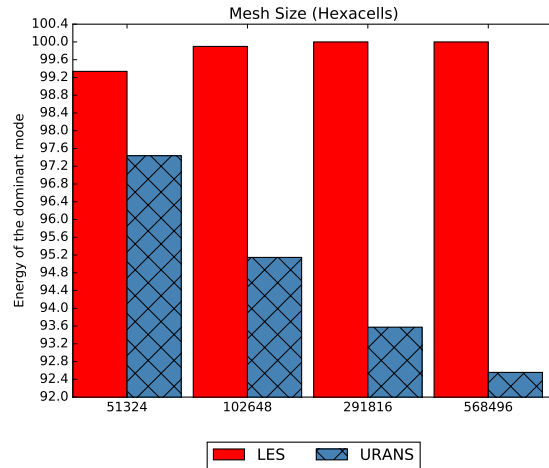


FIGURE 6. Energy contained in dominant mode for LES and URANS (%).

matrix of $N_u^{rn} = 10 \cdot 10 = 100$, according to (3.1). Finally, the POD is applied on the weighted global matrix and the same procedure as in standard POD is followed. The final decay of the eigenvalues can be seen in figure (7). For the purposes of the comparison, the same number of modes for both the standard POD and the nested POD have been chosen. This makes $N_u^r = 14$, $N_p^r = N_{sup}^r = 7$, $N_\theta^r = 9$ and $N_{\nu_t}^r = 8$. The numerical effort of the nested POD can be calculated as $\mathcal{O}([N_t^3 \cdot N_p + [N_u^{\text{nested}}]^3]) = \mathcal{O}(30^3 \cdot 10 + [10 \cdot 10]^3) \approx 2 \cdot 10^6$, while for the standard POD $\mathcal{O}([N_t^3 \cdot N_p + [N_u^{\text{nested}}]^3]) = \mathcal{O}([30 \cdot 10]^3) \approx 2 \cdot 10^7$. Therefore, the nested POD is one order of magnitude faster. For cases with a higher number of snapshots and sampling points, the smaller numerical effort of the nested POD is more apparent, see for example the results in [12].

In the online phase, the ROM is evaluated in a new set of values $U_m = 0.132$ m/s and $U_b = 0.264$ m/s which belong in the training manifold but they differ from the training samples. The ROM is simulated for 3s with timestep $dt = 0.0025$ s as well. For the FOM, the total execution time is 3403.22s while for the ROM 11.02s. This sets the ROM approximately 309 times faster than the FOM.

In figure (8), the relative ϵ_{L^2} error between the FOM and the ROM constructed using standard POD and nested POD methods is shown. This is calculated as:

$$(43) \quad \epsilon_{L^2}(t) = \frac{\|X_{FOM}(t) - X_{ROM}(t)\|_{L^2(\Omega)}}{\|X_{FOM}(t)\|_{L^2(\Omega)}} \%$$

According to this figure, the relative error in the case of standard POD method is slightly lower during the first half of the simulation followed by similar or slightly better performance of the nested POD during the second half. Tables (6) and (7) summarise a few statistics, showing minimum, maximum and average error for nested and standard POD methods, where, the average error is similar for both cases,

respectively. A visualisation of the fields is shown in figures (9,10 and 11) for time instances $t = 0.5$ s, 1.5s and 3s. The difference between the FOM and ROM field is also visualised in figure (13). The biggest difference between the FOM and ROM fields is found in the mixing area of the pipe. This behaviour is expected as in the mixing region the flow is complex and is changing in time. This behaviour is also shown in figure (16), where the radial velocity is plotted against the arc length of the pipe in three regions: before the mixing, in the mixing and after the mixing region, close to the outlet. The mixing region is where the radial velocity diverges the most. For the temperature fields, figure (10) shows that, during the beginning of the simulation, the ROM is slightly more diffusive than the FOM. Since the flow in the inlets is not fully turbulent at the start of the simulation, the extra contribution of the eddy viscosity field bases functions could cause this behaviour. As the flow becomes turbulent, this phenomenon is not anymore apparent. The pressure field appears to have the largest relative error according to figures (8) and (13). This can be attributed to the lack of an explicit equation for pressure, as in the ROM, the pressure bases functions are projected onto the continuity equation using the supremizer method [48, 4]. This affects also the error in velocity field, since the equations for the FOM and ROM are not fully consistent. An exploitation of a Poisson equation for pressure would probably improve the error [39, 16, 54]. The energy equation is still weakly coupled with the momentum equation, therefore the error appears smaller for temperature field. The eddy viscosity field of the FOM, ROM with nested POD and ROM with standard POD is shown in figure (12), as well as their relative error and 11) for time instances $t = 0.5$ s, 1.5s and 3s. The difference between the FOM and ROM field is also visualised in figure (14), where appear to be in good agreement. To further assess the performance of the ROM against the FOM, the relative error

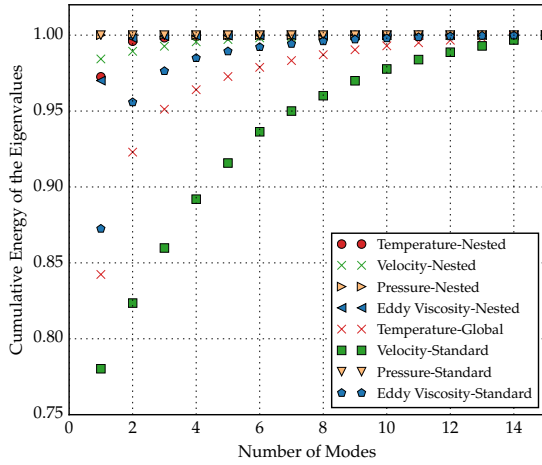


FIGURE 7. Cumulative energy of the eigenvalues for temperature, velocity, pressure and eddy viscosity fields for nested and standard POD methods, respectively.

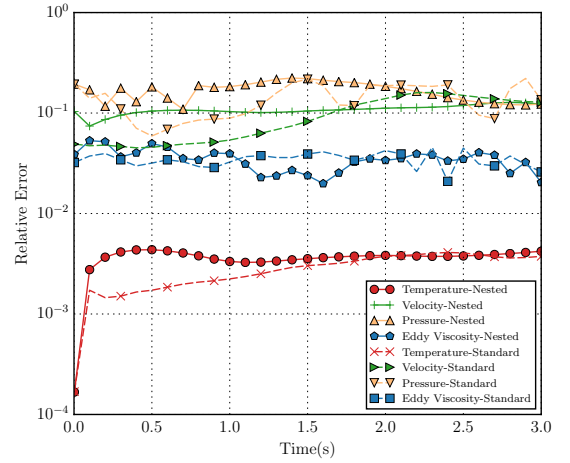


FIGURE 8. $\epsilon_{L^2}(t)$ error for temperature, velocity, pressure and eddy viscosity fields for the nested and standard POD methods, respectively.

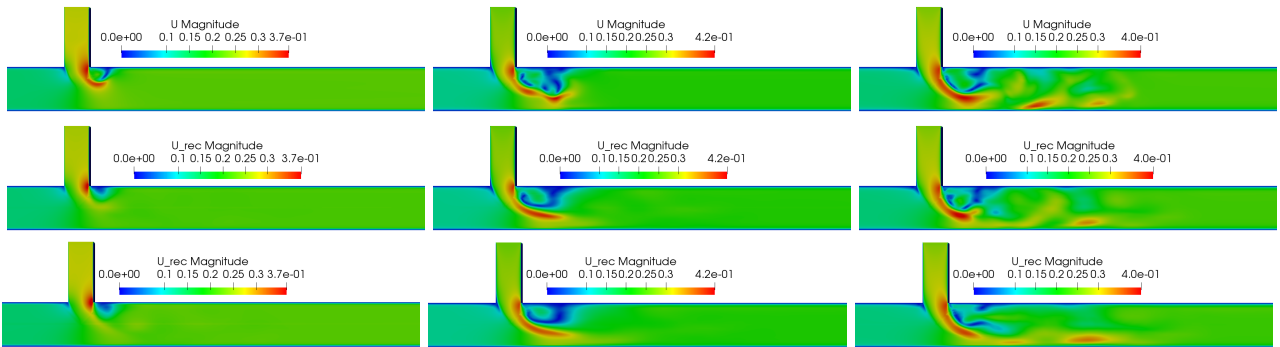


FIGURE 9. Comparison of the velocity field for the full order (first row) and reduced order model using standard POD (second row) and nested POD method (third row). The fields are depicted for different time instances equal to $t = 0.5s, 1.5s$ and $3s$ and increasing from left to right.

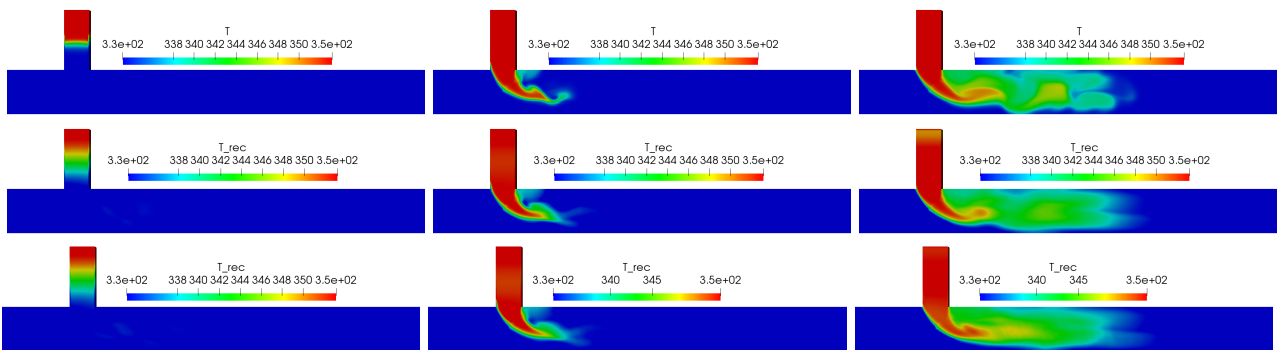


FIGURE 10. Comparison of the temperature field for the full order (first row) and reduced order model using standard POD (second row) and nested POD method (third row). The fields are depicted for different time instances equal to $t = 0.5s, 1.5s$ and $3s$ and increasing from left to right.

	FOM	ROM
$\partial/\partial t$	Backward	Backward
$\nabla \cdot$	Upwind, Central	Upwind, Central
∇^2	Central	Central

TABLE 4. Numerical Schemes for FOM and ROM.

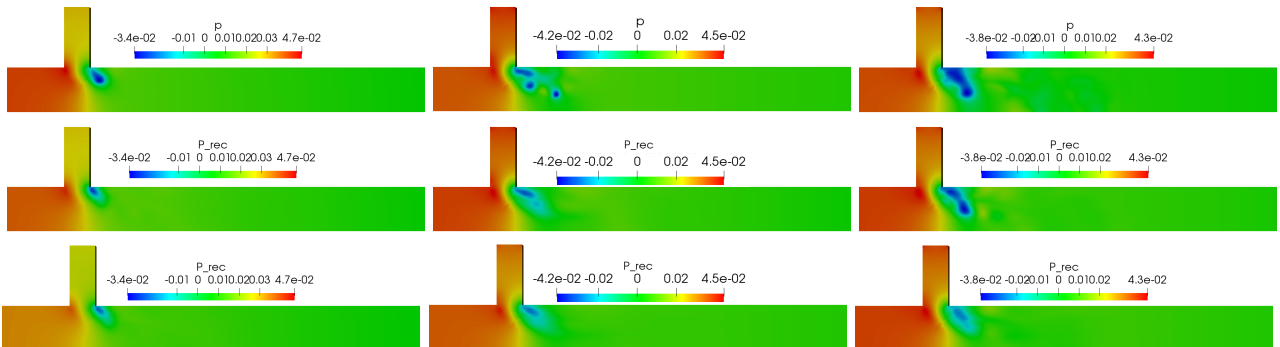
U_m (m/s)	U_b (m/s)
0.08	0.16
0.09	0.18
0.10	0.20
0.11	0.22
0.12	0.24
0.13	0.26
0.14	0.28
0.15	0.30
0.16	0.32
0.17	0.34

TABLE 5. Sampling points for the parameters.

Nested	\mathbf{u}	θ	p	ν_t
Minimum	0.074	0.00016	0.109	0.0199
Maximum	0.128	0.004	0.223	0.0531
Average	0.108	0.0036	0.168	0.0348

TABLE 6. Relative $\epsilon_{L^2}(t)$ error for velocity, temperature and pressure and eddy viscosity fields for the nested POD method.

Standard	\mathbf{u}	θ	p	ν_t
Minimum	0.045	0.00016	0.059	0.0209
Maximum	0.160	0.00418	0.2210	0.0455
Average	0.094	0.0028	0.1398	0.0346

TABLE 7. Relative $\epsilon_{L^2}(t)$ error for velocity, temperature and pressure and eddy viscosity fields for two the standard POD method.FIGURE 11. Comparison of the pressure field for the full order (first row) and reduced order model using standard POD (second row) and nested POD method (third row). The fields are depicted for different time instances equal to $t = 0.5s, 1.5s$ and $3s$ and increasing from left to right.

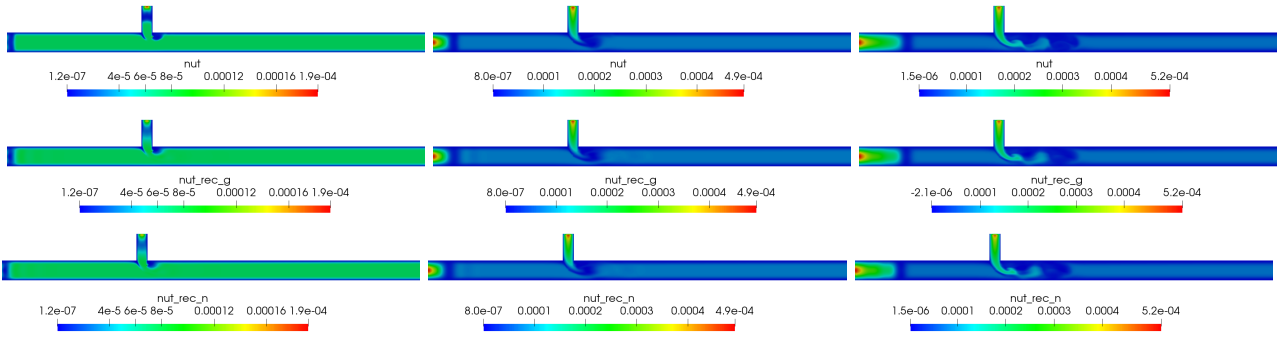


FIGURE 12. Comparison of the eddy viscosity field for the full order (first row) and reduced order model (second row) using the standard POD method. The fields are depicted for different time instances equal to $t = 0.5s, 1.5s$ and $3s$ and increasing from left to right.

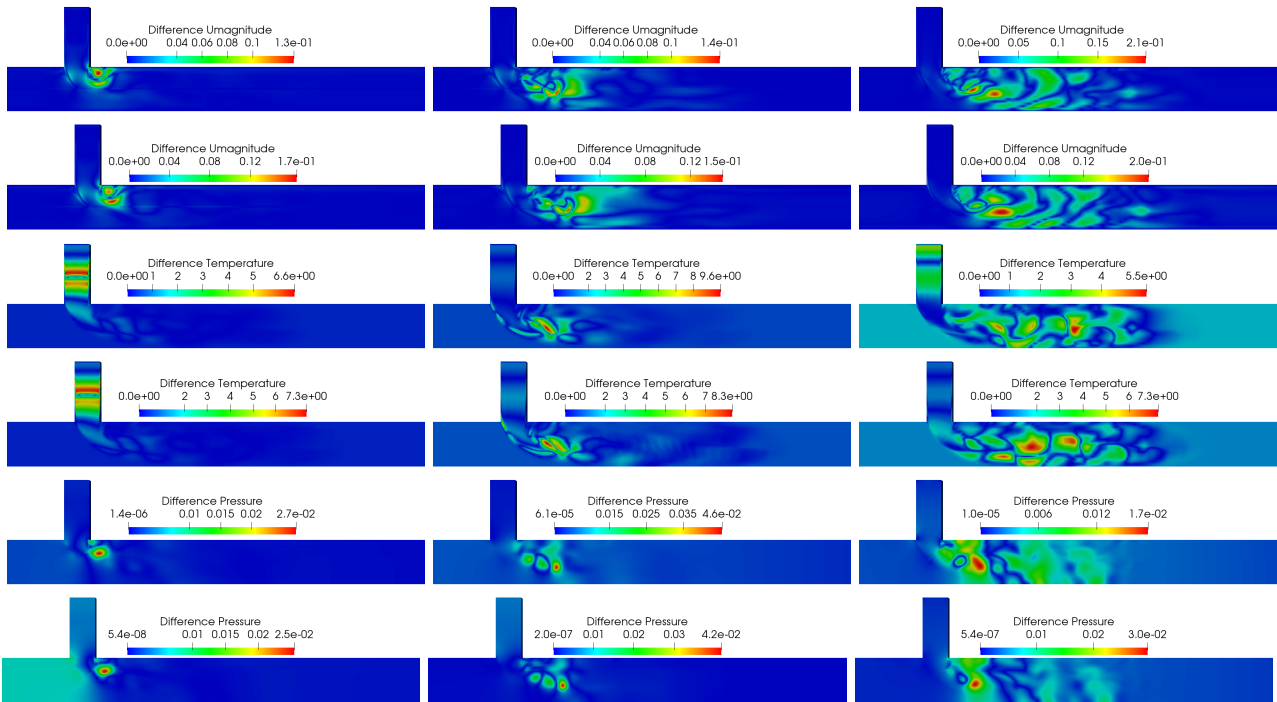


FIGURE 13. Difference between the full order and reduced order standard POD (odd rows) and nested POD (even rows) for velocity, temperature and pressure fields, respectively. The fields are depicted for different time instances equal to $t = 0.5s, 1.5s$ and $3s$ and increasing from left to right.

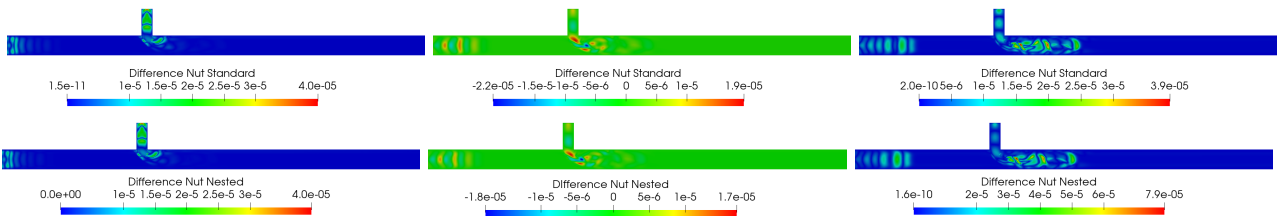


FIGURE 14. Difference between the full order and reduced order standard POD (first three rows) and nested POD (last three rows) for the eddy viscosity field. The fields are depicted for different time instances equal to $t = 0.5s, 1.5s$ and $3s$ and increasing from left to right.

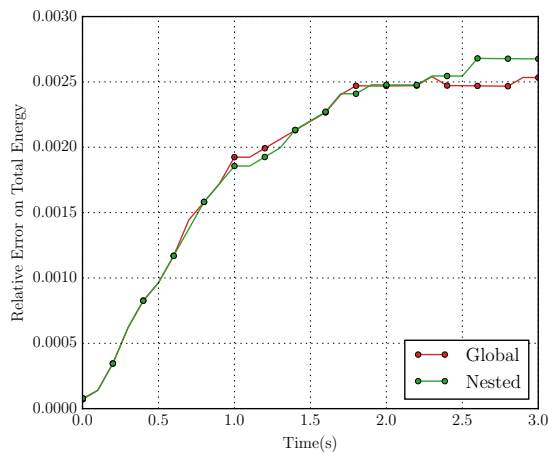


FIGURE 15. Relative error on total energy (kinetic and thermal) between the FOM and the ROM for standard and nested POD methods.

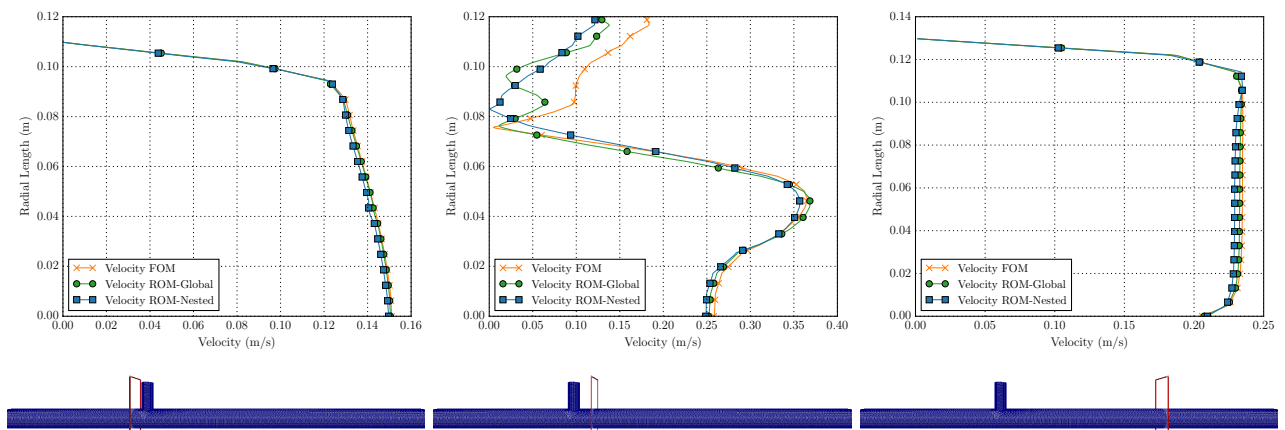


FIGURE 16. Comparison of the radial velocity between the FOM, ROM-Global and ROM-Nested for three different locations, before the mixing, in the mixing region and near the outlet for $t = 3s$. The second row depicts the locations where the sampling takes place.

	FOM	ROM
CPU (s)	3403.22	11.02

TABLE 8. Computational time for the full order and reduced order models.

of the total energy (kinetic and thermal) is plotted in figure (15), where it shows a small (less than 0.3%) but increasing with time relative error. As POD-Galerkin method is known to show some instabilities with long time integration, this behaviour is expected. This is also apparent in figure (8), where the relative error grows with time.

5. CONCLUSION

In this work a hybrid reduced order model for modelling turbulent heat transfer problems has been studied. The

hybrid method consists of POD-Galerkin approach for the velocity, temperature and pressure fields and POD-RBF for the eddy viscosity field. Furthermore, two variations of POD, standard and nested, have been studied and compared. For the study of the decay of the POD modes, LES and URANS simulations have also been compared. The proposed method is tested for a T-junction pipe where turbulent thermal mixing takes place. According to the results, the ROM constructed using standard or nested POD is capable of reproducing the FOM results with good accuracy,

in both cases. The relative error between the FOM and ROM, which peaks in the mixing region, is within acceptable levels, from engineering point of view. A speed-up factor of approximately 309 has been calculated, meaning that the ROM is two orders of magnitude faster than the FOM. Regarding the comparison between the LES and URANS, it has been found that, unlike URANS, LES needs only a single eddy viscosity POD mode for well resolved meshes.

As future suggestions, adding the two way coupling between velocity and temperature equations would result to a ROM which could model more realistic industrial flows [56]. As turbulent flow is highly complex in nature, to enhance the results and reduce the relative error, a method where local ROMs are constructed for each value of the sampling parameter and then interpolated would probably result in a more accurate ROM and would be of great interest.

ACKNOWLEDGEMENTS

We acknowledge the financial support of Rolls-Royce, EPSRC, the European Research Council Executive Agency by means of the H2020 ERC Consolidator Grant project AROMA-CFD “Advanced Reduced Order Methods with Applications in Computational Fluid Dynamics” - GA 681447, (PI: Prof. G. Rozza) and INdAM-GNCS 2019.

APPENDIX A. LIST OF ABBREVIATIONS AND SYMBOLS

Abbreviations

PODI	Proper Orthogonal Decomposition with Interpolation
POD	Proper Orthogonal Decomposition
RBF	Radial Basis Functions
ROM	Reduced Order Model

Symbols

\bar{u}	mean velocity field
$\bar{\theta}$	mean temperature field
\bar{p}	mean pressure field
α	reduced vector of unknowns for velocity
∇	gradient operator
$\nabla \cdot$	divergence operator
$\nabla \times$	curl operator
∇^s	symmetric gradient operator
D^R	Reynolds-averaged strain rate tensor
Θ	Radial Basis Function kernels
φ_i	i-th POD basis function for velocity
b	reduced vector of unknowns for pressure
c	reduced vector of unknowns for temperature
f	Dirichlet boundary condition for velocity
G	ROM convection matrix for the heat equation
h	initial condition for velocity
I	Identity matrix
K	ROM mass matrix for the heat equation
l	reduced vector of unknowns for eddy viscosity
M	ROM mass matrix
N	ROM diffusion matrix for the heat equation
n	outward normal vector
P	ROM pressure gradient matrix
Q	ROM convection tensor
Q_{T1}	ROM turbulent tensor
Q_{T2}	ROM turbulent tensor
u	velocity field
u'	fluctuating velocity field
U_s	Snapshot matrix
U^i	i-th nested snapshot matrix
U_{sn}^{nested}	Global snapshot matrix resulting from nested POD
W	eigenvector matrix
w	Vector of weights
Δ	laplacian operator
ϵ	Dissipation rate
ϵ_{L^2}	Relative error

γ	Spread of a kernel
$\langle \cdot, \cdot \rangle$	inner product in $L^2(\Omega)$
$\ \cdot\ $	norm in $L^2(\Omega)$
\mathcal{K}	training set space
\mathcal{P}	parameter space
ω	Specific dissipation rate
\otimes	tensor product
τ^R	Reynolds stress tensor
θ'	fluctuating temperature field
ζ	Control functions
C	correlation matrix
e	initial condition for temperature
g	Dirichlet boundary condition for temperature
H^R	Heat flux term
k	Turbulent kinetic energy
N_t	number of time instances
p'	fluctuating pressurefield
Q	space-time domain
T	final time
u_D	Scaling coefficients
α_{dif_t}	turbulent thermal diffusivity
α_{dif}	thermal diffusivity
χ_i	i-th POD basis function for temperature
ϵ_{L^2}	L^2 norm error
Γ	boundary of Ω
ν_t	eddy viscosity
ν	dimensionless kinematic viscosity
Ω	bounded domain
ψ_i	i-th POD basis function for pressure
θ	temperature field
ξ_i	i-th POD basis function for eddy viscosity
N_p^s	number of unknowns for pressure at reduced order level before the truncation
N_u^h	number of degrees of freedom for velocity at full-order level
N_u^r	number of unknowns for velocity at reduced order level after the truncation
N_u^s	number of unknowns for velocity at reduced level before the truncation
N_μ	number of parameters in the training set \mathcal{K}
N_θ^s	number of unknowns for temperature at reduced order level before the truncation
Pr_t	turbulent Prandtl number
p	pressure field

REFERENCES

1. *OpenFOAM website*, <https://openfoam.org/>, Accessed: 13-10-2017.
2. Hseyin Ayhan and Cemal Niyazi Skmen, *CFD modeling of thermal mixing in a T-junction geometry using les model*, Nuclear Engineering and Design **253** (2012), 183 – 191, SI : CFD4NRS-3.
3. Francesco Ballarin, Elena Faggiano, Sonia Ippolito, Andrea Manzoni, Alfio Quarteroni, Gianluigi Rozza, and Roberto Scrofani, *Fast simulations of patient-specific haemodynamics of coronary artery bypass grafts based on a PODGalerkin method and a vascular shape parametrization*, Journal of Computational Physics **315** (2016), 609 – 628.
4. Francesco Ballarin, Andrea Manzoni, Alfio Quarteroni, and Gianluigi Rozza, *Supremizer stabilization of POD-Galerkin approximation of parametrized steady incompressible Navier-Stokes equations*, International Journal for Numerical Methods in Engineering **102** (2014), no. 5, 1136–1161.
5. Francesco Ballarin, Andrea Manzoni, Alfio Quarteroni, and Gianluigi Rozza, *Supremizer stabilization of POD-Galerkin approximation of parametrized steady incompressible Navier-Stokes equations*, International Journal for Numerical Methods in Engineering **102** (2015), no. 5, 1136–1161.
6. Francesco Ballarin and Gianluigi Rozza, *PODGalerkin monolithic reduced order models for parametrized fluid-structure interaction problems*, International Journal for Numerical Methods in Fluids **82**, no. 12, 1010–1034.

7. J. Baltzer, R. Adrian, and X. Wu, *Turbulent boundary layer structure identification via POD*, Proceedings of the summer program, 2010, p. 55.
8. Matthew F. Barone, Irina Kalashnikova, Daniel J. Segalman, and Heidi K. Thornquist, *Stable Galerkin reduced order models for linearized compressible flow*, Journal of Computational Physics **228** (2009), no. 6, 1932 – 1946.
9. Peter Benner, Serkan Gugercin, and Karen Willcox, *A survey of projection-based model reduction methods for parametric dynamical systems*, SIAM Review **57** (2015), 483–531.
10. S. Bernero and H. E. Fiedler, *Application of particle image velocimetry and proper orthogonal decomposition to the study of a jet in a counterflow*, Experiments in Fluids **29** (2000), no. 7, S274–S281.
11. Rmi Bourguet, Marianna Braza, and Alain Dervieux, *Reduced-order modeling of transonic flows around an airfoil submitted to small deformations*, Journal of Computational Physics **230** (2011), no. 1, 159 – 184.
12. Benjamin Brands, Julia Mergheim, and Paul Steinmann, *Reduced-order modelling for linear heat conduction with parametrised moving heat sources*, GAMM-Mitteilungen **39** (2016), no. 2, 170–188.
13. AG Buchan, CC Pain, F Fang, and IM Navon, *A pod reduced-order model for eigenvalue problems with application to reactor physics*, International Journal for Numerical Methods in Engineering **95** (2013), no. 12, 1011–1032.
14. T. Bui-Thanh, *Proper orthogonal decomposition extensions and their applications in steady aerodynamics*, Master thesis, Master thesis, High Performance Computation for Engineered Systems, Singapore-MIT Alliance, 2003.
15. Saray Busto, Giovanni Stabile, Gianluigi Rozza, and Mara Elena Vzquez-Cendn, *POD-Galerkin reduced order methods for combined Navier-Stokes transport equations based on a hybrid FV-FE solver*, Computers & Mathematics with Applications, Accepted (2018).
16. Alfonso Caiazzo, Traian Iliescu, Volker John, and Svetlana Schyschlowa, *A numerical investigation of velocity-pressure reduced order models for incompressible flows*, Journal of Computational Physics **259** (2014), 598 – 616.
17. Kevin Carlberg, Charbel Bou-Mosleh, and Charbel Farhat, *Efficient non-linear model reduction via a least-squares Petrov-Galerkin projection and compressive tensor approximations*, International Journal for Numerical Methods in Engineering **86** (2010), no. 2, 155–181.
18. Kevin Carlberg, Charbel Farhat, Julien Cortial, and David Amallem, *The GNAT method for nonlinear model reduction: Effective implementation and application to computational fluid dynamics and turbulent flows*, Journal of Computational Physics **242** (2013), 623 – 647.
19. F. Chinesta, A. Huerta, G. Rozza, and K. Willcox, *Model Order Reduction*, Encyclopedia of Computational Mechanics, Elsevier Editor, 2016 (2016).
20. Francisco Chinesta, Pierre Ladeveze, and Elías Cueto, *A Short Review on Model Order Reduction Based on Proper Generalized Decomposition*, Archives of Computational Methods in Engineering **18** (2011), no. 4, 395.
21. L. Cordier and M. Bergmann, *Proper Orthogonal Decomposition: an overview*, Lecture series 2002-04, 2003-03 and 2008-01 on post-processing of experimental and numerical data, Von Karman Institute for Fluid Dynamics, 2008., VKI, 2008, p. 46 pages.
22. Mehdi Dehghan and Mostafa Abbaszadeh, *Proper orthogonal decomposition variational multiscale element free Galerkin (POD-VMEFG) meshless method for solving incompressible navier-stokes equation*, Computer Methods in Applied Mechanics and Engineering **311** (2016), 856–888.
23. Valentina Dolci and R. Arina, *Proper orthogonal decomposition as surrogate model for aerodynamic optimization*, 2016.
24. A. Dumon, C. Allery, and A. Ammar, *Proper general decomposition (PGD) for the resolution of Navier-Stokes equations*, Journal of Computational Physics **230** (2011), no. 4, 1387–1407.
25. Th. Frank, C. Lifante, H.-M. Prasser, and F. Menter, *Simulation of turbulent and thermal mixing in T-junctions using urans and scale-resolving turbulence models in ANSYS CFX*, Nuclear Engineering and Design **240** (2010), no. 9, 2313 – 2328, Experiments and CFD Code Applications to Nuclear Reactor Safety (XCFD4NRS).
26. S Georgaka, G Stabile, G Rozza, and M.J. Bluck, *Parametric POD-Galerkin model order reduction for unsteady-state heat transfer problems*, Communications in Computational Physics (2018).
27. W. R. Graham, J. Peraire, and K. Y. Tang, *Optimal control of vortex shedding using low-order models. Part I: open-loop model development*, International Journal for Numerical Methods in Engineering **44** (1999), no. 7, 945–972.
28. Bernard Haasdonk, *Convergence rates of the POD-Greedy method*, ESAIM: Mathematical Modelling and Numerical Analysis **47** (2013), no. 3, 859–873.
29. Saddam Hijazi, Shafqat Ali, Giovanni Stabile, Francesco Ballarin, and Gianluigi Rozza, *The Effort of Increasing Reynolds Number in Projection-Based Reduced Order Methods: from Laminar to Turbulent Flows*, 2018.
30. Saddam Hijazi, Giovanni Stabile, Andrea Mola, and Gianluigi Rozza, *Data-driven POD-Galerkin reduced order model for turbulent flows*, submitted (2019).
31. Khac Chi Hoang, Pierre Kerfriden, BC Khoo, and SPA Bordas, *An efficient goal-oriented sampling strategy using reduced basis method for parametrized elastodynamic problems*, Numerical Methods for Partial Differential Equations **31** (2015), no. 2, 575–608.
32. R.I Issa, *Solution of the implicitly discretised fluid flow equations by operator-splitting*, Journal of Computational Physics **62** (1986), no. 1, 40 – 65.
33. I. Kalashnikova and M. F. Barone, *On the stability and convergence of a Galerkin reduced order model (ROM) of compressible flow with solid wall and far-field boundary treatment*, International Journal for Numerical Methods in Engineering **83** (2010), no. 10, 1345–1375.
34. A.K. Kuczaj, E.M.J. Komen, and M.S. Loginov, *Large-eddy simulation study of turbulent mixing in a T-junction*, Nuclear Engineering and Design **240** (2010), no. 9, 2116–2122 (English).
35. Stefano Lorenzi, Antonio Cammi, Lelio Luzzi, and Gianluigi Rozza, *POD-Galerkin method for finite volume approximation of navier-stokes and RANS equations*, Computer Methods in Applied Mechanics and Engineering **311** (2016), 151–179.
36. John Leask Lumley, *The structure of inhomogeneous turbulent flows*, Atmospheric turbulence and radio wave propagation (1967).
37. F. Moukalled, L. Mangani, and M. Darwish, *The Finite Volume Method in Computational Fluid Dynamics: An Advanced Introduction with OpenFOAM and Matlab*, 1st ed., Springer Publishing Company, Incorporated, 2015.
38. V.S. Naik-Nimbalkar, A.W. Patwardhan, I. Banerjee, G. Padmakumar, and G. Vaidyanathan, *Thermal mixing in T-junctions*, Chemical Engineering Science **65** (2010), no. 22, 5901 – 5911.
39. Bernd R. Noack, Paul Papas, and Peter A. Monkewitz, *The need for a pressure-term representation in empirical Galerkin models of incompressible shear flows*, Journal of Fluid Mechanics **523** (2005), 339–365.
40. Z. Ostrowski, R. A. Bialecki, and A. J. Kassab, *Solving inverse heat conduction problems using trained pod-rbf network inverse method*, Inverse Problems in Science and Engineering **16** (2008), no. 1, 39–54.
41. Alfio Quarteroni, Andrea Manzoni, and Federico Negri, *Reduced Basis Methods for Partial Differential Equations*, Springer International Publishing, 2016.

42. Arun Prakash Raghupathy, Urmila Ghia, Karman Ghia, and William Maltz, *Boundary-condition-independent reduced-order modeling of complex 2d objects by POD-galerkin methodology*, 2009 25th Annual IEEE Semiconductor Thermal Measurement and Management Symposium, IEEE, 2009.
43. Ritesh R. Rama, Sebastian Skatulla, and Carlo Sansour, *Real-time modelling of diastolic filling of the heart using the proper orthogonal decomposition with interpolation*, International Journal of Solids and Structures **96** (2016), 409 – 422.
44. S. S. Ravindran, *A reduced-order approach for optimal control of fluids using proper orthogonal decomposition*, International Journal for Numerical Methods in Fluids **34** (2000), no. 5, 425–448.
45. Dietmar Rempfer and Hermann F. Fasel, *Evolution of three-dimensional coherent structures in a flat-plate boundary layer*, Journal of Fluid Mechanics **260** (1994), no. -1, 351.
46. Clarence W. Rowley, Tim Colonius, and Richard M. Murray, *Model reduction for compressible flows using {POD} and Galerkin projection*, Physica D: Nonlinear Phenomena **189** (2004), no. 12, 115 – 129.
47. G. Rozza, D. B. P. Huynh, and A. T. Patera, *Reduced Basis Approximation and a Posteriori Error Estimation for Affinely Parametrized Elliptic Coercive Partial Differential Equations*, Archives of Computational Methods in Engineering **15** (2008), no. 3, 229.
48. Gianluigi Rozza and Karen Veroy, *On the stability of the reduced basis method for Stokes equations in parametrized domains*, Computer Methods in Applied Mechanics and Engineering **196** (2007), no. 7, 1244 – 1260.
49. F. Salmoiraghi, A. Scardigli, H. Telib, and G. Rozza, *Free-form deformation, mesh morphing and reduced-order methods: enablers for efficient aerodynamic shape optimisation*, International Journal of Computational Fluid Dynamics **32** (2018), no. 4-5, 233–247.
50. Alberto Sartori, Antonio Cammi, Lelio Luzzi, and Gianluigi Rozza, *A reduced basis approach for modeling the movement of nuclear reactor control rods*, Journal of Nuclear Engineering and Radiation Science **2** (2016), no. 2, 021019.
51. Lawrence Sirovich, *Turbulence and the Dynamics of Coherent Structures part I: Coherent Structures*, Quarterly of Applied Mathematics **45** (1987), no. 3, 561–571.
52. G. Stabile and G. Rozza, *ITHACA-FV - In real Time Highly Advanced Computational Applications for Finite Volumes*, Accessed: 2018-01-30.
53. Giovanni Stabile, Francesco Ballarin, Giacomo Zuccarino, and Gianluigi Rozza, *A reduced order variational multiscale approach for turbulent flows*, Advances in Computational Mathematics, Accepted (2019).
54. Giovanni Stabile, Saddam Hijazi, Andrea Mola, Stefano Lorenzi, and Gianluigi Rozza, *POD-Galerkin reduced order methods for CFD using Finite Volume Discretisation: vortex shedding around a circular cylinder*, Communications in Applied and Industrial Mathematics **8** (2017), no. 1, 210–236.
55. Giovanni Stabile and Gianluigi Rozza, *Finite volume POD-Galerkin stabilised reduced order methods for the parametrised incompressible Navier-Stokes equations*, Computers & Fluids (2018).
56. K Star, G Stabile, S Georgaka, F Belloni, G Rozza, and J Degroot, *POD-Galerkin Reduced Order Model of the Boussinesq Approximation for Buoyancy-Driven Enclosed Flows*, Proceedings of International Conference on Mathematics and Computational Methods applied to Nuclear Science and Engineering, Portland, Oregon USA, 2019, 2019.
57. R. Tunstall, D. Laurence, R. Prosser, and A. Skillen, *Large eddy simulation of a T-junction with upstream elbow: The role of Dean vortices in thermal fatigue*, Applied Thermal Engineering **107** (2016), 672 – 680.
58. Karsten Urban, Stefan Volkwein, and Oliver Zeeb, *Greedy sampling using nonlinear optimization*, Reduced Order Methods for modeling and computational reduction, Springer, 2014, pp. 137–157.
59. H. K. Versteeg and W. Malalasekera, *An Introduction to Computational Fluid Dynamics. The Finite Volume Method*, Longman Group Ltd., London, 1995.
60. C. Walker, M. Simiano, R. Zboray, and H.-M. Prasser, *Investigations on mixing phenomena in single-phase flow in a T-junction geometry*, Nuclear Engineering and Design **239** (2009), no. 1, 116 – 126.
61. David C Wilcox et al., *Turbulence modeling for cfd*, vol. 2, DCW industries La Canada, CA, 1998.
62. D Xiao, F Fang, J Du, CC Pain, IM Navon, AG Buchan, AH ElSheikh, and G Hu, *Non-linear petrov-galerkin methods for reduced order modelling of the navier-stokes equations using a mixed finite element pair*, Computer Methods In Applied Mechanics and Engineering **255** (2013), 147–157.
63. D Xiao, F Fang, CC Pain, IM Navon, P Salinas, and A Mugeridge, *Non-intrusive reduced order modeling of multi-phase flow in porous media using the POD-RBF method*, J. Comput. Phys. (2015).